Songklanakarin J. Sci. Technol.
43 (4), 1152-1159, Jul. - Aug. 2021

http://www.sjst.psu.ac.th

Original Article

Near surface electrical resistivity structures around an active fault trace in Weh Island, Indonesia

Nanda Muhammad[1], Rizal Syamsul[1, 2], Abdullah Faisal[3], Idroes Rinaldi[1, 4], and Ismail Nazli[3*]

[1] *Graduate School of Mathematics and Applied Sciences, Universitas Syiah Kuala, Banda Aceh, 23111 Indonesia*

[2] *Department of Marine Sciences, Faculty of Marine and Fisheries, Universitas Syiah Kuala, Banda Aceh, 23111 Indonesia*

[1] *Department of Physics, Faculty of Mathematics and Natural Sciences, Universitas Syiah Kuala, Banda Aceh, 23111 Indonesia*

[4] *Department of Chemistry, Faculty of Mathematics and Natural Sciences, Universitas Syiah Kuala, Banda Aceh, 23111 Indonesia*

Received: 20 May 2020; Revised: 26 August 2020; Accepted: 1 September 2020

Abstract

Near-surface investigation has been carried out in Cot Abeuk, Weh Island, Indonesia. The area is part of the Seulimeum segment active fault, the northernmost branch of the Great Sumatran Fault. We measured two parallel electrical resistivity tomography profiles on the area with the direction perpendicular to the fault strike. The length of profile 1 and profile 2 are 111 m and 125 m, respectively, with 1 meter spacing between electrodes. Along the Profile 2, VLF-EM and Geomagnetic data were also acquired for complementary. The 2D inverted resistivity models show some minor fractures, which can be related to ruptures in the past. The structure was made by weathering rocks, clay and andesite. The models align with the analytic signal of total magnetic field anomalies as well as in-phase, Fraser filter and conductivity model derived from VLM-EM data. Following the successful models, this location is a potential candidate for paleo-seismological excavation.

Keywords: shallow structure, rapture, Seulimeum Segment, Great Sumatran Fault, paleo-seismic

1. Introduction

The active fault zone is an area with a high potential for hazards such as earthquake, tsunami, and other destructive hazards. These hazards may cause disasters if they occur close to community settlements. As a country located above the plate tectonic border, Indonesia has many active fault systems which intersect with densely populated settlements, for example the Great Sumatra Fault (GSF) system. The GSF is a dextral strike-slip fault system which extends along Sumatra Island to the Andaman sea for almost 1900 km length. The fault breaks into ~19 segments with irregular structures (Sieh & Natawidjaja, 2000). In the northernmost part, the GSF splits in two segments, which are Aceh and Seulimeum segments. The last segment extends across the Weh Island at the northern waters of Sumatra and continues to the Andaman sea (Figure 1).

The Seulimeum Segment is as an active fault (Muksin *et al.*, 2018) although there have been no major earthquake events for almost 200 years along the segment (Bellier *et al.*, 1997; Sieh & Natawidjaja, 2000). This seismic gap may produce an earthquake with magnitude about 7.4 in

*Corresponding author
Email address: nazli.ismail@unsyiah.ac.id

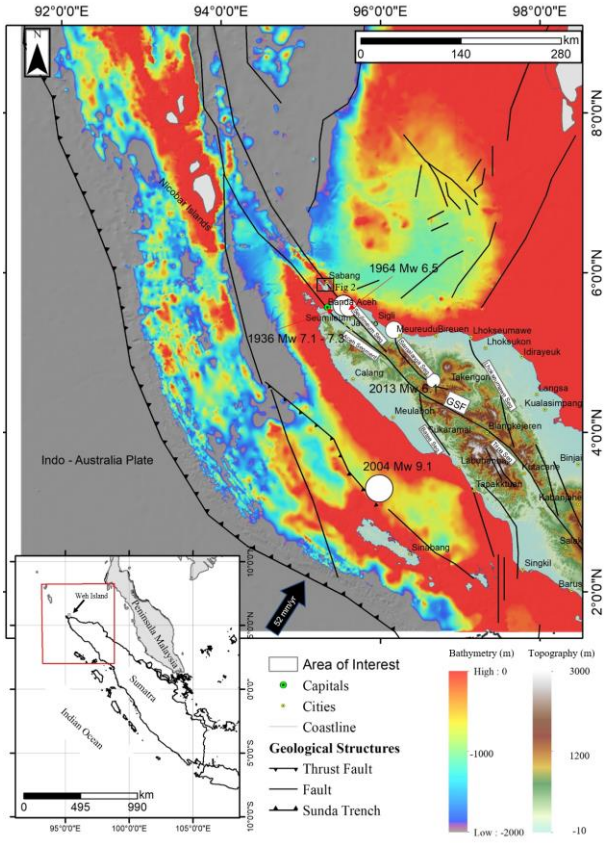

Figure 1. Overview map showing faults, geological structures, and plate boundaries (modified from Curray, 2005). The topography and bathymetry backgrounds are based on ASTER 30x30 m data and SRTM 15plus, respectively. The white circle indicates the location of historical destructive earthquakes recorded in the region.

the future (Ito *et al.*, 2012). Therefore, studies further on seismic hazards along the fault are important since the fault line passes highly populated areas in Aceh Province, i.e. Banda Aceh as a capital city and Weh Island as industrial area in the province.

Seismic activities along an active fault zone can induce ruptures as well as minor fault structures (Wei, He, Su, Zhuang, & Sun, 2019). The ruptures are essential for paleo-seismological experts because they contain long-term information. By examining the historical seismic ruptures, we can make a prediction related to geological structure, fault displacement, time of events and earthquake magnitudes (Roquero *et al.*, 2019). Based on this reason, we present a near-surface geological structure along the active fault derived from geophysical data measurement to provide basic information about the area prior to paleo-seismic excavation. Few paleo-seismological studies have been done along the Seulimeum segment (e.g. Ismail, Yanis, Idris, Abdullah, & Hanafiah, 2015). Some studies were focused on historical earthquakes produced by the subduction zones along the West Coast of Sumatra (e.g. Kelsey *et al.*, 2015; Sieh *et al.*, 2015).

Paleo-seismic excavations are practically ineffective, costly, and time-consuming (Wei *et al.*, 2019). We need to know the exact position of the rapture before the trenching. Fault traces mapping is done commonly through satellite imagery interpretation and geomorphic observation fields. Both methods rely on information from the surface only. Therefore, subsurface data obtained based on geophysical survey will be able to enrich the information. Application integrated geophysical methods can produce high-resolution data for shallow-depth studies (Karcıoğlu, 2019). There are many geophysical methods that can be used for shallow-depth studies such as VLF-EM (e.g. Yanis, Bakar, & Ismail, 2017), geomagnetic (e.g. Asyqari, Sugiyanto, Yanis, & Ismail, 2019), ERT (e.g. Berge, 2014), and the combination of several geophysical methods (e.g. Bastani, Malehmir, Ismail, Pedersen, & Hedjazi, 2009). In this paper, we integrate VLF EM, geomagnetic, and ERT methods for shallow-depth studies in Cot Abeuk Village, Weh Island (Figure 2).

2. Geological Setting

Weh Island is situated in the Andaman Sea, close to the northern tip of Sumatra (Figure 1). The main island has an area of 156.3 km^2 with 15 km length and 10 km width. This island is a stratovolcano composed of volcanic rocks (Barber, Crow, & Milsom, 2005). The last eruption occurred during Pleistocene or lower Quaternary period. Volcanic lava units and pyroclastic flows dominantly cover the island from the Quaternary period (Dirasutisna & Hasan, 2005). Andesitic and basaltic lava occupy approximately 58%. Volcanoclastic rocks consisting of sandy tuff and laharic breccias comprise approximately 30%. The rest are reef Limestone at the northeastern area, hydrothermally influencing rocks around geothermal field and alluvium along the coastal area (Kurnio, Syafri, Sudradjat, Rosana, & Muslim, 2015).

Topographically, the area is characterized by high reliefs of undulating mountain and steep hills as a result of erosion and fault activities. The main fault with NW-SE direction is an extension of the Seulimeum Segment. This fault was formed in the early Tertiary period (Dirasutisna & Hasan, 2005). As part of the GSF, the extension of Seulimeum fault on Weh Island is also the lateral strike-slip fault. Tectonically, the fault system is subjected by relative motion between Indo-Australia and Eurasia Plates (Genrich *et al.*, 2000).

3. Methods and Data Acquisition

Data acquisition was carried out in a valley area in Cot Abeuk Village, located 4 km from the city of Sabang to the southeast (Figure 2). The site was selected based on National DEM (DEMNAS) satellite image (BIG, 2018) interpretation and geomorphic field observation that showed both fault location as well as strike direction in northeast-southeast. Two profiles of ERT data were acquired with the direction perpendicular to the strike, while the VLF-EM and geomagnetic data were acquired only along one profile for complementary. Table 1 presents information related to data acquisition in this study.

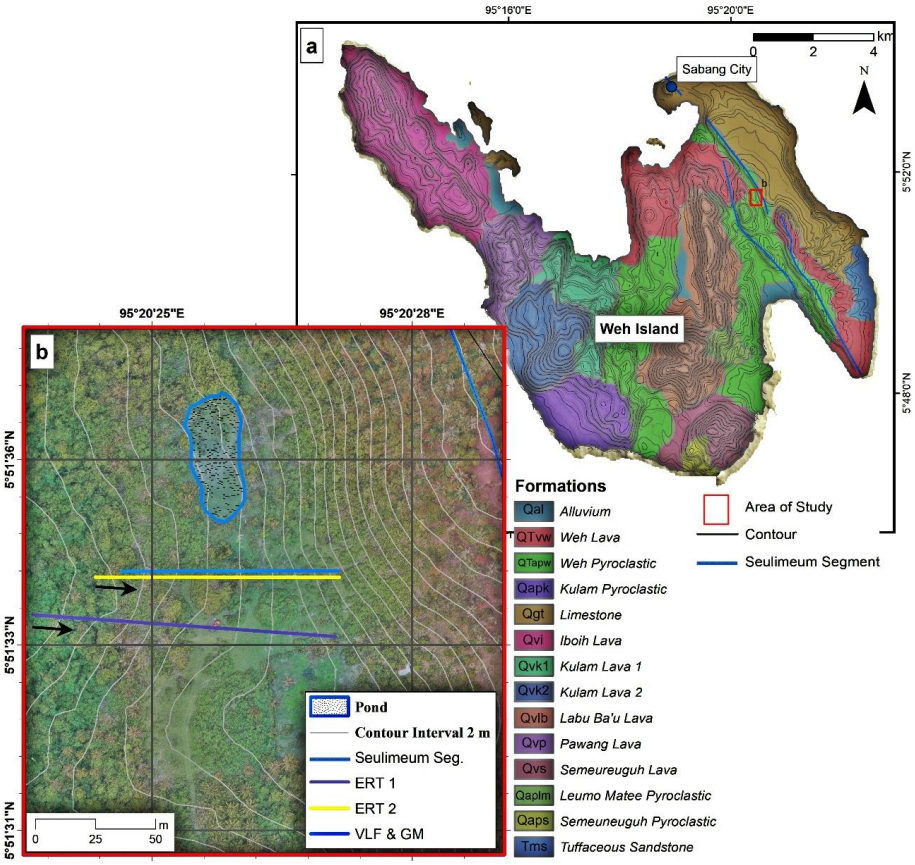

Figure 2 (a) The study area of Weh island overlaid by geological maps (modified based on Dirasutisna & Hasan, 2005) and geomorphological maps based on a satellite image DEMNAS (Badan Informasi Geospasial [BIG], 2018), (b) Profiles sketch of geophysical data acquisition

Table 1. Data acquisition parameters

No	Parameter	Data
1	ERT	
	Number of profiles	2
	Sampling spacing	1 m
	Total length	236 m
2	Geomagnetic	
	Number of profiles	1
	Sampling spacing	1 m
	Total length	90 m
3	VLF – EM	
	Number of profiles	1
	Sampling spacing	1 m
	Total length	90 m
	Frequencies used	17,4 kHz

3. 1 Electrical Resistivity Tomography (ERT)

The distance between ERT profiles, namely profile 1 and profile 2 is about 20 m with 111 m and 125 m length, respectively. The data were measured using SuperSting R8 resistivity/IP meter instrument (Figure 3b) (Advanced Geosciences, 2011) with Wenner-Schlumberger arrays.

In principle, the measurement was conducted by injecting current using two direct current (DC) electrodes into the ground. The two other electrodes measured the voltage between the current electrodes along the profiles. Distribution of apparent resistivity (ρ_a) data within the subsurface was calculated using Equation (1) (Loke, Chambers, Rucker, Kuras, & Wilkinson, 2013) as:

$$\rho_a = K\frac{\Delta V}{I}, \quad (1)$$

where K is geometric factors, I is isotropic injected current, and V is voltage. The geometrical factor is defined as (Loke, 2002):

$$K = \pi n(n+1)a\,, \quad (2)$$

the geometrical factor defines the correction of magnitude from two current potential electrodes with the order of electrodes (n) and spacing between two electrodes (a).

We used 2D inversion code of Res2dinv for modeling (Loke & Barker, 1996; Loke, 2002). The method is based on L2 smoothness-constrained least-squares method. The best model is obtained by choosing the smallest root

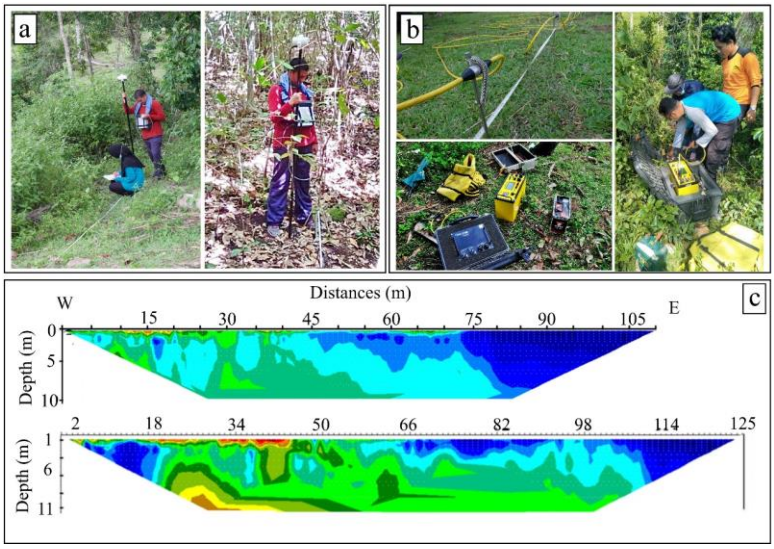

Figure 3. Field view of research site with data acquisition process (a) Geomagnetic and VLF-EM acquisition (b) ERT acquisition (c) Raw data ERT profile 1 (d) Raw data ERT profile 2

mean square (RMS) error value between the measured and calculated apparent resistivity data (Zhang, Liu, Ai, & Qin, 2014) in Equation 3.

$$RMS = \sqrt{\frac{1}{N}\sum\left(\frac{d_i - f_i(m)}{\varepsilon_i}\right)^2}, \quad (3)$$

N is the number of measurements, d is the data measurement, $f(m)$ is forward modelled data and ε is the required tolerance, where $i = 1, 2, 3, \ldots, N$.

3. 2 VLF-EM method

The VLF EM method is one of the fast and powerful methods used in shallow studies (Sundararajan, Babu, Prasad, & Srinivas, 2006). Resistivity contrast from VLF-EM results can optimally interpret fault zones boundary and fracture zones (Zarif *et al.*, 2018). In the VLF-EM method, a military navigation transmitter with a low-frequency signal (15-30 kHz) is used for electromagnetic field source. Secondary magnetic field will be detected on the surface with the presence of conductors or resistors within the subsurface (Gnaneshwar, Shivaji, Srinivas, Jettaiah, & Sundararajan, 2011).

In this study, the GEM system of GSM19 Series (GEM System, 2008) was used for VLF – EM data measurement (Figure 3a). 1m spacing between stations was used during data collection for improving the resolution of shallow surface structures (Figure 2b). The data were measured at frequency of 17.4 kHz transmitted by Japan's VLF NDT transmitter station. The measurements of horizontal (H_x) and vertical (H_z) magnetic fields were used to calculate tilt angle (α) and ellipticity (e) values. Real (in-phase) and imaginary (quadrature) components can be used in KHFFILT program. These components are based on the tilt angle and ellipticity as: Re = tan (α) × 100% and Im = e × 100% (Pirttij, 2004).

A qualitative interpretation was carried out using the linear filter Fraser technique (Fraser, 1969). This technique converts non-contourable to contourable data and reduces noise in the data so that it can calculate the limit of an anomaly of interpretation (Sundararajan *et al.*, 2006).

$$F_{2,3} = (M_3 + M_4) - (M_1 + M_2), \quad (4)$$

where $F_{2,3}$ is the point between M_2 and M_3. Continually, $F_{i,i+1}$ is generated from M_i and M_{i+1}. Meanwhile, M_1, M_2, M_3, M_4 are the four continuous measurement points (Fraser, 1969). The Fraser filter shifts the cross points between real and imaginary data into positive peaks marked as anomalies.

The Karous-Hjelt filter (Karous & Hjelt, 1983) was used to determine the apparent depth and position of the anomaly. The VLF-EM signal is filtered at station intervals, which is then linked to SD between measurement points.

$$\frac{\Delta z}{2\pi} I_a\left(\frac{\Delta x}{2}\right) = -0.205H_{-2} + 0.323H_{-1} - 1.446H_0 + 1.466H_1 - 0.323H_2 + 0.205H_3, \quad (5)$$

where Δz is depth (m), I_a = is the apparent current density (%), Δx = measurement space (m), and H is tilt angle data (%).

3. 3 Geomagnetic method

Total magnetic field data were collected along the same profile of the VLF-EM. Proton Precession Magnetometer (PPM) GEM 19 with a sensitivity reaching 0.1 nT (GEM System, 2008) were used for data acquisitions (Figure 3a). Diurnal and International Geomagnetic Reference Field (IGRF) corrections were performed to the measured total magnetic field data. The data after correction are called total magnetic field anomaly which are caused by the magnetic body of the target (Reynolds, 1997).

Further filtering of analytic signal method has been applied to the magnetic field anomaly data (Blakely, 1996). The analytic signal (*AS*) transformation can simplify the total magnetic field (*T*) anomalies measured at low geomagnetic latitude as we measured in this study. The analytic signal data are calculated as the square root of the sum of the vertical-horizontal derivatives and two orthogonal of the magnetic field (Debeglia & Corpel, 1997).

$$As\ (x, y) = \sqrt{\left(\frac{\partial T}{\partial x}\right)^2 + \left(\frac{\partial T}{\partial z}\right)^2} \qquad (6)$$

4. Results and Discussion

Figure 4a and Figure 4b shows inverted resistivity models of profile 1 dan profile 2, respectively. The inverted model in profile 1 and profile 2 reached an RMS data fit of 2% and 2.6%, respectively, after six iterations. The profiles show irregular layers. There are some disturbances and undulations along the western part of the profiles due to surface slope. In general, both models show three layers of subsurface based on resistivity distributions, especially along the eastern part of the profiles. The uppermost layer is dominated by low resistivity values (i.e. <35 Ohm-m, blue). Below this conductivity layer, the medium resistivity value layer (i.e. 35 - 68 Ohm-m, green) is superimposed by layers with relatively high resistivity values (i.e. above 70 Ohm-m, yellow-brown).

A very thin medium to high resistivity layer covers the surface with thickness of about 1 to 2 m along the west side of Profile 1. This layer is interpreted as gravels mixed with top soil which is relatively dry. More gravel deposit is found along the slope accumulated by erosion process from the hill at east side of the profile, especially along Profile 1. This layer is superimposed by most conductive material continuously found along the profile. At the eastern part along the profile, this layer is very dominant. The medium to high resistivity layer is found again at the deeper part of the profiles. However, some discontinuities with vertical changes occurred along the profile.

The conductive zone represented by the low resistivity layer is interpreted as sediment from weathering rock (i.e. wet clay, sand, until pumice). The thickness of this layer ranges from 1 to 10 m. The conductive layer can be affected by water content since we found a pond at the northern side of the area. The accumulation of sediments in this area (east side of each profile) is assumed to be the result of sediment transport originating from the hill on the east side (Figure 2). Rock weathering occurs because of the reduction in rock mass strength. This process results in disintegration and decomposition of the material (Luo, Xu, Ren, Wang, & Gao, 2020).

The medium resistivity layer is interpreted as clay, whereas the highly resistive values are interpreted as andesite rocks. Based on geomorphological observations in the field, some andesite fractions are also found on the surface. It is predicted as a result of erosion from several piles of andesite on the west side, while geomorphic observation on the east side shows loose soil (i.e. clay and sand). The vertical discontinuities found along this layer are probably caused by minor fault. They can be related to seismicity events in the past.

The predicted minor fault along the inverted resistivity model is also revealed by total magnetic field anomaly data with signal analytic transformation (Figure 5a). Some peaks of signal analytic profile coincided with vertical discontinuity of the inverted resistivity models along Profile 2. However, the existence of the minor faults will be not clear when the signal analytic profile is interpreted alone without being compared with other methods.

The measured VLF – EM data consist of in-phase (real component) and out-phase (imaginary component). The VLF – EM used the low frequency of radio electromagnetic signal with high noise content. The noise could be caused by error in data acquisition process or geological noises (Everett & Weiss, 2002). Moving average filter or smoothing process is commonly used to reduce noise content in the measured data (Bovik, 2009). The real and imaginary components of the measured data after the application of moving average filter are shown in Figure 5b. Both data are superimposed. Presence of conductor within subsurface can be interpreted by intersection between the real and imaginary component (Sundararajan *et al.*, 2006; Osinowo & Falufosi, 2018). However, the inspections are not clear enough in our data set.

Complexity of geological structures beneath the surface may interfere with the secondary fields, making it difficult to interpret data (Osinowo & Falufosi, 2018). In order to simplify the interpretation, Fraser (1969) introduced a filter that shifts the data 90°. The filter transforms the anomaly such that those parts with the maximum slope appear with the maximum amplitude of current density. The calculated Fraser filter is shown in Figure 5c. The profile shows peaks of current density at distances 35, 45, 55, 60, 66, 80, 82, 85, 100, 110, 114 dan 120 m along the profile that can be interpreted as location of conductor (Gnaneshwar *et al.*, 2011). The peaks also coincide with the anomalies found in analytic signal of total magnetic field data and the inverted resistivity model along Profile 2. Although it is based on profile anomaly and monogram, the VLV-EM method has commonly been used for shallow structures investigation (e.g. Saydam, 1981).

Qualitative interpretation of the VLF – EM data on KHHFILT is shown in Figure 5d. Based on the real component (Figure 5b, dotted black line), the model shows apparent current density distribution with pseudo depth along the profile. The KHHFILT filter also shows high current density values at distance 35, 45, 55, 60, 66, 80, 82, 85, 100, 110, 114 and 120 m along the profile. The conductor shown in Figure 5d are better than the current densities shown in Figure 4c since it already includes the pseudo depth. The maximum conductivities can be interpreted as the existence of the fracture ruptures (Jamal & Singh, 2018; Karcıoğlu, 2019).

Figures 5d and Figure 5e show a good agreement about the presence of minor faults along the profile, parallelly. Length of the inverted model of the ERT profile (Figure 5e) is longer than the KHHFILT profile (Figure 5d), therefore some minor faults are missing along the VLF-EM. The Fraser data (Figure 5c) also show similar information since the data are also derived from VLF-EM data. With some exception, the analytic signal of total magnetic field anomalies (Figure 5a) also show the presence of the faults, but they could not be able to resolve the structures clearly. While the real and imaginary components of the VLF-EM data (Figure 5b) cannot be interpreted directly as the existence of the minor faults, therefore, further transformation processes such as Fraser

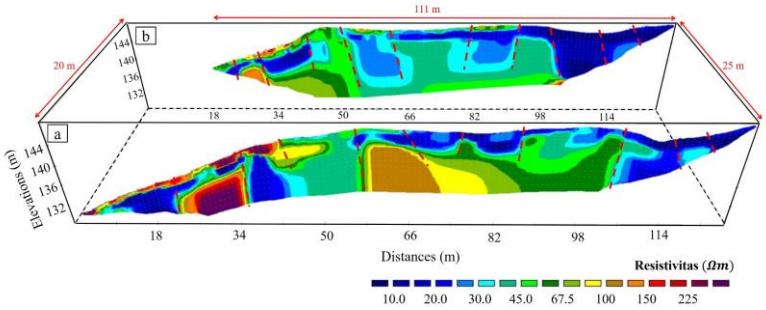

Figure 4. 3D views of the 2D ERT models of (a) profile 1 and (b) profile 2. The red dashed line shows the interpretation of the existence of rapture.

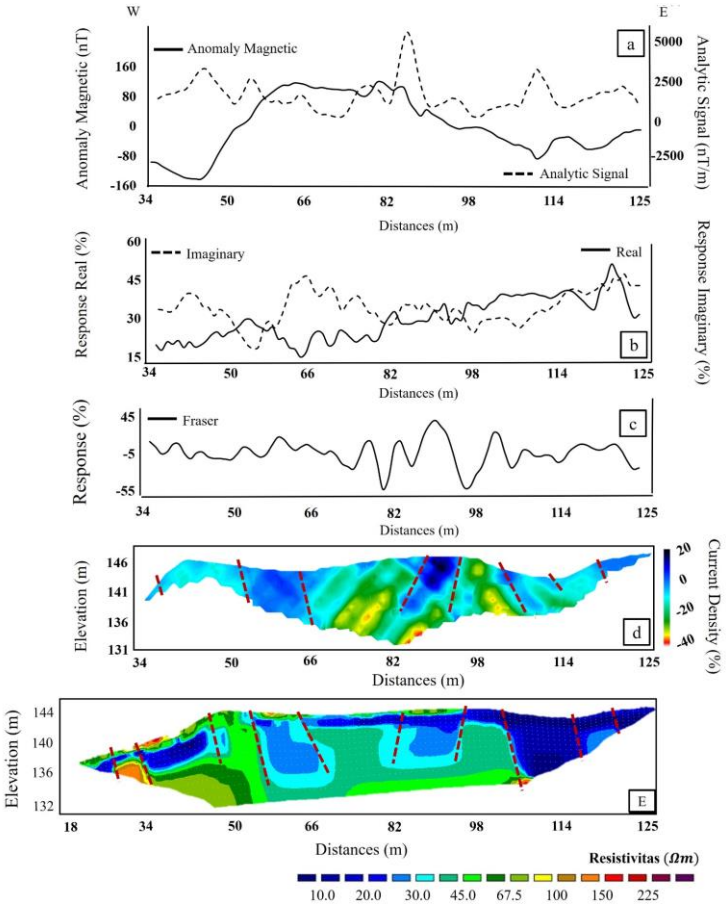

Figure 5. Comparison data and model of Profile 2 derived from geomagnetic, VLF – EM and ERT methods (a) Total anomaly and Signal analytical geomagnetic, (b) In-phase and out-phase component VLF EM, (c) Fraser filter, (d) filter KHFFILT, and (e) ERT inverted model.

(Figure 5c) and KHHFILT (Figure 5d) and are needed. Based on the interpretation, profile 2 shows more detail structures than the other one. Therefore, location of the excavation should be along profile 2 in the form of the trench with length 125 m and depth up to 10 m.

5. Conclusions

Based on satellite image interpretation and field geomorphic observations, at the study area of Cot Abeuk, Weh Island, some fault traces of active fault were found. The geophysical methods have provided a better understanding of near surface geological structures of the area. 2D inverted resistivity model indicates that the subsurface structure consists of clay, sand, sedimentary weathered rocks, and andesite. The ERT method, with electrodes spacing 1 m, can provide optimal results in mapping shallow structures associated as fractures, minor faults or raptures. However, in terms of data acquisition, this method is more challenging compared to other geophysical methods applied in this study. Practically, the geomagnetic and VLF-EM methods are faster and easier. However, their data cannot be used for

straightforward interpretation, especially the geomagnetic method in this study. Nevertheless, the data and models presented by the geomagnetic, VLF-EM and ERT methods can potentially be used for a preliminary method of paleo-seismic study. Based on the findings, the excavation should be done along the profile 2. Further excavation at the area will provide a better understanding about geological records of past large earthquakes which occurred along the Seulimeum segment of GSF extension.

Acknowledgements

The authors would like to thank the Ministry of Research, Technology and Higher Education for funding this research through PMDSU research grant, with a contract number: 70/UN11.2/PP/SP3/2018.

References

Advanced Geosciences, I. (2011). *Instruction manual for supersting earth resistivity, IP and SP system powersting external high power transmitters*. Austin, TX: Author.

Asyqari, A., Sugiyanto, D., Yanis, M., & Ismail, N. (2019). Mapping of archaeological structure along east-coast of Aceh Besar District, Indonesia based on total magnetic field anomalies Mapping of archaeological structure along east-coast of

Aceh Besar District, Indonesia based on total magnetic field anomalies. *IOP Conference Series: Earth and Environmental Science*, *348*. doi:10.1088/1755-1315/348/1/012041

Badan Informasi Geospasial. (2018). Seamless Digital Elevation Model (DEM) dan Batimetri Nasional. Retrieved from http://tides.big.go.id/DEMNAS/

Barber, A. J., Crow, M. J., & Milsom, J. S. (2005). *Sumatra, Geological Society Memoir* (31st ed., Vol. 31). London, England: The Geological Society. doi:10.1017/CBO9781107415324.004

Bastani, M., Malehmir, A., Ismail, N., Pedersen, L. B., & Hedjazi, F. (2009). Delineating hydrothermal stockwork copper deposits using controlled-source and radio-magnetotelluric methods: A case study from northeast Iran. *Geophysics*, *74*(5). doi:10.1190/1.3174394

Bellier, O., Michel, S., Pramumijoyo, S., Beaudouin, T., Harjono, H., Bahar, I., & Forni, O. (1997). Paleoseismicity and seismic hazard along the Great Sumatran Fault (Indonesia). *Journal of Geo dynamics*, *24*(1–4), 169–183. doi:10.1016/S0264-3707(96)00051-8

Berge, M. A. (2014). Electrical resistivity tomography investigations on a paleoseismological trenching study. *Journal of Applied Geophysics*, *109*, 162–174. doi:10.1016/j.jappgeo.2014.07.022

Blakely, R. J. (1996). *Potential theory in gravity and magnetic applications*. Cambridge, England: Cambridge University Press.

Bovik, A. (2009). *The essential guide to image processing*. Austin, TX: Department of Electrical and Computer Engineering, The University of Texas at Austin. doi:10.1016/B978-0-12-374457-9.X0001-7

Curray, J. R. (2005). Tectonics and history of the Andaman Sea region. *Journal of Asian Earth Sciences*, *25*, 187–232. doi:10.1016/j.jseaes.2004.09.001

Debeglia, N., & Corpel, J. (1997). Automatic 3-D interpretation of potential field data using analytic signal derivatives. *Geophysics*, *62*(1), 87–96. doi:10.1190/1.1444149

Dirasutisna, S., & Hasan, R. (2005). Geology of Jaboi Geothermal Area. *Unpublished Report of Center for Geological Resources, Geological Agency of Indonesia, Bandung, Indonesian*, 1–18.

Everett, M. E., & Weiss, C. J. (2002). Geological noise in near-surface electromagnetic induction data. *Geo physical Research Letters*, *29*(1), 2–5. doi:10.1029/2001GL014049

Fraser, D. C. (1969). Contouring of VLF - EM Data. *Geophysics*, *34*(6), 959–967. doi:10.1190/1.1440065

GEM System Inc. (2008). Instruction manual GSM 19 v.7.0. Advanced Magnetometers, Ontario, Canada: Author. Retrieved from https://userpage.fu-berlin.de/geodyn/instruments/Manual_GEM_GSM-19.pdf

Genrich, J. F., Bock, Y., McCaffrey, R., Prawirodirdjo, L., Stevens, C. W., Puntodewo, S. S. O., . . . Wdowinski, S. (2000). Distribution of slip at the northern Sumatran fault system. *Journal of Geophysical Research: Solid Earth*, *105*(B12), 28,327-28,341. doi:10.1029/2000JB900158

Gnaneshwar, P., Shivaji, A., Srinivas, Y., Jettaiah, P., & Sundararajan, N. (2011). Verylow-frequency electromagnetic (VLF-EM) measurements in the Schirmacheroasen area, East Antarctica. *Polar Science*, *5*(1), 11–19. doi:10.1016/j.polar.2010.09.001

Ismail, N., Yanis, M., Idris, S., Abdullah, F., & Hanafiah, B. (2015). Near-surface fault structures of the seulimuem segment based on electrical resistivity model. *Journal of Physics: Conference Series*, *846*, 012016. doi:10.1088/1742-6596/846/1/012016

Ito, T., Gunawan, E., Kimata, F., Tabei, T., Simons, M., Meilano, I., . . . Sugiyanto, D. (2012). Isolating along-strike variations in the depth extent of shallow creep and fault locking on the northern Great Sumatran Fault Isolating along-strike variations in the depth extent of shallow creep and fault locking on the northern Great Sumatran Fault, (June). doi:10.1029/2011JB008940

Jamal, N., & Singh, N. P. (2018). Identification of fracture zones for groundwater exploration using very low frequency electromagnetic (VLF-EM) and electrical resistivity (ER) methods in hard rock area of Sangod Block, Kota District, Rajasthan, India. *Groundwater for Sustainable Development*. doi:10.1016/j.gsd.2018.05.003

Karcıoğlu, G. (2019). Near-surface resistivity structure near avcilar landslide in İstanbul, Turkey by 2D inversion of VLF data. *Journal of Applied Geophysics*. doi:10.1016/j.jappgeo.2019.02.012

Karous, M., & Hjelt, S. E. (1983). Linear filtering of VLF Dip - Angle measurements. *Geophysical Prospecting*, *31*, 782–794. doi:10.1111/j.1365-2478.1983.tb01085.x

Kelsey, H. M., Engelhart, S. E., Pilarczyk, J. E., Horton, B. P., Rubin, C. M., Daryono, M. R., . . . Cahill, N. (2015). Accommodation space, relative sea level, and the archiving of paleo-earthquakes along subduction zones. *Geology*, *43*(8), 1–4. doi:10.1130/G36706.1

Kurnio, H., Syafri, I., Sudradjat, A., Rosana, M. F., & Muslim, D. (2015). Seafloor faulting and its relation to submarine volcanic activities based on sub bottom profiling (SBP) analyses in Weh Island waters and its surrounding, Nangroe Aceh Darussalam Province. *Bulletin of the Marine Geology*, *30*(1), 1–10. doi:10.32693/bomg.30.1.2015.70

Loke, M. H. (2002). *Tutorial: 2-D and 3-D electrical imaging surveys*. Retrieved from https://sites.ualberta.ca/~unsworth/UA-classes/223/loke_course_notes.pdf

Loke, M. H., & Barker, R. D. (1996). Rapid least-squares inversion of apparent resistivity pseudosections by a quasi-Newton method. *Geophysical Prospecting*, *44*, 131–152. doi:10.1111/j.1365-2478.1996.tb00142.x

Loke, M. H., Chambers, J. E., Rucker, D. F., Kuras, O., & Wilkinson, P. B. (2013). Recent developments in the direct-current geoelectrical imaging method. *Journal of Applied Geophysics*, *95*, 135–156. doi:10.1016/j.jappgeo.2013.02.017

Luo, J., Xu, Z., Ren, Z., Wang, K., & Gao, H. (2020). Quantitative assessment of weathering degree of Touzhai rock- avalanche deposit in Southwest China. *Geomorphology*, *359*, 107162. doi:10.1016/j.geomorph.2020.107162

Muksin, U., Irwandi, Rusydy, I., Muzli, Erbas, K., Marwan, . . . Ismail, N. (2018). Investigation of Aceh segment and Seulimeum fault by using seismological data; a preliminary result. *Journal of Physics: Conference Series*, *1011*, 012031. doi:10.1088/1742-6596/1011/1/012031

Osinowo, O. O., & Falufosi, M. O. (2018). Magnetic and very low frequency electromagnetic (VLF-EM) investigations for gold exploration around Ihale in Bunnu-Kabba Area of Kogi, north-central Nigeria. *Contributions to Geophysics and Geodesy*, *48*(3), 191–205. doi:10.2478/congeo-2018-0008

Pirttij, M. (2004). Karous-Hjelt and Fraser filtering of VLF measurements. *Geophisical Prospective*, *31*(5), 782-794.

Reynolds, J. M. (1997). *An introduction to applied and environmental geophysics*. Wales, England: Reynolds Geo-Sciences.

Roquero, E., Silva, P. G., Rodríguez-pascua, M. A., Bardají, T., Elez, J., Carrascogarcía, P., & Giner-robles, J. L. (2019). Geomorphology analysis of faulted fan surfaces and paleosols in the Palomares Fault Zone (Betic Cordillera, SE Spain): Paleoclimatic and paleoseismic implications. *Geomorphology*, *342*, 88–102. doi:10.1016/j.geomorph.2019.06.003

Saydam, A. S. (1981). Very low-frequency electromagnetic interpretation using tilt angle and ellipticity measurements. *Geophysics*, *46*(1), 1594–1605. doi:10.1190/1.1441166

Sieh, K., Daly, P., Edwards McKinnon, E., Pilarczyk, J. E., Chiang, H., Horton, B., . . .Feener, R. M. (2015). Penultimate predecessors of the 2004 Indian Ocean tsunami in Aceh, Sumatra: Stratigraphic, archeological, and historical evidence. *Journal of Geophysical Research: Solid Earth*, *120*(1), 308–325. doi:10.1002/2014JB011538

Sieh, K., & Natawidjaja, D. (2000). Neotectonics of the Sumatran fault, Indonesia. *Journal of Geophysical Research*. doi:10.1029/2000JB900120

Sundararajan, N., Babu, V. R., Prasad, N. S., & Srinivas, Y. (2006). Short Note VLFPROS — A Matlab code for processing of VLF-EM data. *Computers and Geosciences*, *32*, 1806–1813. doi:10.1016/j.cageo.2006.02.021

Wei, Z., He, H., Su, P., Zhuang, Q., & Sun, W. (2019). Geomorphology investigating paleoseismicity using fault scarp morphology of the Dushanzi Reverse Fault in the northern Tian Shan, China. *Geomorphology*, *327*, 542–553. doi:10.1016/j.geomorph.2018.11.025

Yanis, M., Bakar, A. M., & Ismail, N. (2017). The use of VLF-EM and electromagnetic induction methods for mapping the ancient fort of Kuta Lubok as Tsunami Heritage. *Conference and Exibition EAGE, Near Surface Geoscience*.

Zarif, F., Slater, L., Mabrouk, M., Youssef, A., Al-temamy, A., & Mousa, S. (2018). Groundwater resources evaluation in calcareous limestone using geoelectrical and VLF-EM surveys (El Salloum Basin, Egypt).

Zhang, Y., Liu, D., Ai, Q., & Qin, M. (2014). 3D modeling and inversion of the electrical resistivity tomography using steel cased boreholes as long electrodes. *Journal of Applied Geophysics*. doi:10.1016/j.jappgeo.2014.08.011